Matter and Radiation at Extremes

RESEARCH ARTICLE

scitation.org/journal/mre

Control of electron beam current, charge, and energy spread using density downramp injection in laser wakefield accelerators

Cite as: Matter Radiat. Extremes 8, 024401 (2023); doi: 10.1063/5.0126293
Submitted: 15 September 2022 • Accepted: 30 January 2023 •
Published Online: 15 February 2023

Céline S. Hue,[a] Yang Wan,[a] Eitan Y. Levine, and Victor Malka

AFFILIATIONS

Department of Physics of Complex Systems, Weizmann Institute of Science, Rehovot, Israel

Note: This paper is a part of the Special Topic Collection on Plasma Optics.
[a]**Authors to whom correspondence should be addressed:** celine.hue@weizmann.ac.il and yang.wan@weizmann.ac.il

ABSTRACT

Density downramp injection has been demonstrated to be an elegant and efficient approach for generating high-quality electron beams in laser wakefield accelerators. Recent studies have demonstrated the possibilities of generating electron beams with charges ranging from tens to hundreds of picocoulombs while maintaining good beam quality. However, the plasma and laser parameters in these studies have been limited to specific ranges or attention has been focused on separate physical processes such as beam loading, which affects the uniformity of the accelerating field and thus the energy spread of the trapped electrons, the repulsive force from the rear spike of the bubble, which reduces the transverse momentum $p_\perp$ of the trapped electrons and results in small beam emittance, and the laser evolution when traveling in the plasma. In this work, we present a comprehensive numerical study of downramp injection in the laser wakefield, and we demonstrate that the current profile of the injected electron beam is directly correlated with the density transition parameters, which further affects the beam charge and energy evolution. By fine-tuning the plasma density parameters, electron beams with high charge (up to several hundreds of picocoulombs) and low energy spread (around 1% FWHM) can be obtained. All these results are supported by large-scale quasi-three-dimensional particle-in-cell simulations. We anticipate that the electron beams with tunable beam properties generated using this approach will be suitable for a wide range of applications.

I. INTRODUCTION

Laser wakefield acceleration (LWFA) is one of the most promising accelerator technologies, offering acceleration gradients more than three orders of magnitude higher than conventional accelerators.[1–3] In LWFA,[1] plasma electrons are pushed outward by the ponderomotive force of the intense laser pulse, forming a plasma wave that travels together with the laser pulse at relativistic speeds and is therefore suitable for compact and efficient acceleration of trapped electrons. Numerous injection methods, such as self-injection,[4–8] ionization injection,[9–11] and density downramp injection,[12–15] have been proposed, explored, and demonstrated numerically and experimentally. Over the past few decades, electron injection using a sharp plasma density transition profile[13–15] has been demonstrated to be effective for the generation of high-quality electron beams in LWFA, with plasma electrons being trapped owing to the wave breaking induced by the longitudinal expansion of the plasma wave structure as it propagates along the density downramp. This approach can be easily implemented by inserting a sharp blade on top of the gas nozzle[13,14] and has been used recently to demonstrate free-electron lasing with a high-quality LWFA electron beam of 10–50 pC.[16]

Density downramp injection has been thoroughly studied in the framework of beam-driven plasma wakefield acceleration (PWFA).[17–19] In LWFA, however, the nonlinear laser propagation in the plasma[20,21] makes analysis of the injection mechanism a much more subtle task. This process has been investigated by several groups[22–24] through numerical scans of the downramp parameters. However, very few studies have focused on the current profile of the injected electron beam and its correlation with the beam charge

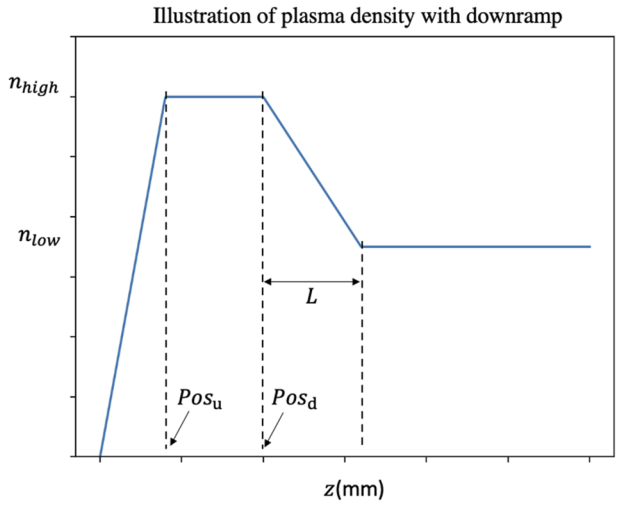

FIG. 1. Plasma density profile used in the study, where the laser pulse propagates along the positive z direction.

and energy properties, although this is of critical importance for many applications, such as the high-efficiency energy gain in a staged LWFA-PWFA scheme that has recently been experimentally demonstrated.[15,25]

In this article, an approach for tailoring the beam current I by tuning the parameters of the plasma density profile (n_{high}, n_{low}, L, and Pos_d) as shown in Fig. 1 is studied by means of numerical simulations performed with the quasi-3D particle-in-cell (PIC) code FBPIC,[26] where the algorithm is based on Fourier–Bessel decomposition of fields on a set of 2D radial grids. It is also explained how the beam current plays a decisive role in tailoring other important beam parameters (charge Q, beam energy E, and energy spread δE).

The laser parameters considered here are typical of laser chains delivering a few tens of terawatts in a few tens of femtoseconds. Here, we took those of the HIGGINS laser system at the Weizmann Institute of Science (WIS),[27] with a pulse duration of 30 fs, a focal spot waist of 18 μm, and a normalized vector potential a_0 of 2.2, corresponding to an on-target laser energy of 1.6 J. The simulations were performed in a cylindrical geometry with two azimuthal modes. We chose a mesh resolution of Δz = 38 nm and Δr = 90 nm in the longitudinal and radial directions, respectively. The results presented here were obtained with 45 particles per mesh cell. In the simulations, the plasma was set to be pre-ionized, which allowed us to study solely the impact of the plasma profile on the injected beam parameters. For all the simulations described in this article, n_{low} was fixed as 2.5×10^{18} cm^{-3} to ensure that the drive laser could be self-guided.[28]

The remainder of this article is organized as follows. We first show in Sec. II how one can tailor the beam current distribution $I(\xi)$ by changing the plasma density parameters, where $\xi = v_g t - z \approx ct - z$ represents the phase inside the wakefield, v_g the laser group velocity in the plasma, and c the speed of light in vacuum. In Sec. III, we discuss the dependence of the beam energy evolution on the beam current $I(\xi)$, and we also report on the achievement of electron beams with energies of hundreds of MeV and charges of hundreds of picocoulombs with relatively good beam quality. In Sec. IV, we explain the maximum limit on the injected beam charge and its effect on the final beam energy and energy spread. We present our conclusions and perspectives in Sec. V.

II. TAILORING THE BEAM CURRENT DISTRIBUTION WITH DIFFERENT PLASMA PROFILES

In this section, we show how one can tailor the beam current distribution $I(\xi)$ by controlling the profiles of the plasma parameters n_{high}, L, and Pos_d. These parameters can be easily tuned experimentally (for example, by changing the positions of blade or string-like obstacles[13,14,29] along the path of the gas jet). Through a series of

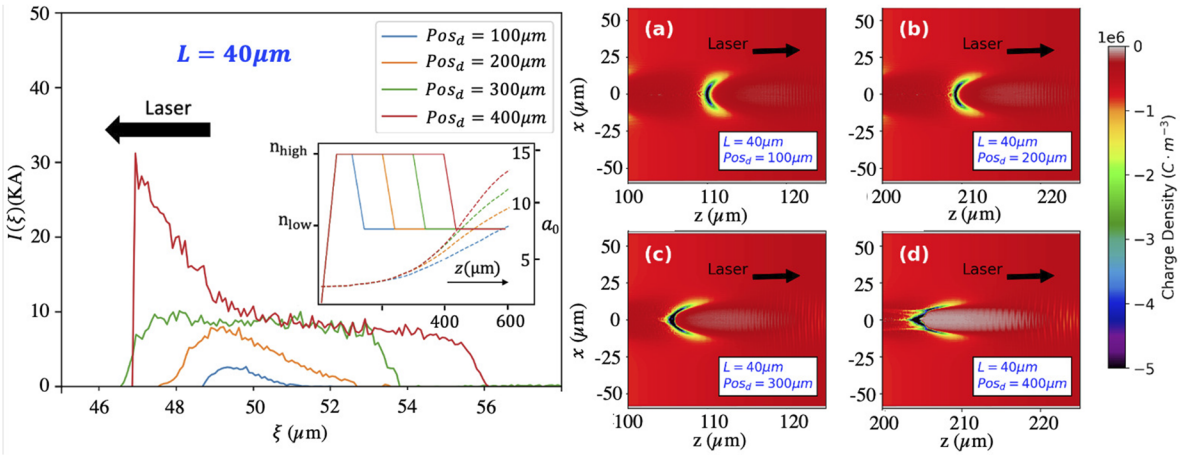

FIG. 2. Left: beam current distribution at the plasma exit for $n_{\text{high}} = 5 \times 10^{18}$ cm^{-3}, $n_{\text{low}} = 2.5 \times 10^{18}$ cm^{-3} and downramp length L = 40 μm. The plasma density and the evolution of the laser vector potential a_0 are shown in the inset. Right: plasma charge density of the wakefield structures at positions where the rear part of the bubble corresponds to the middle of the density downramp.

simulations, it is found that the laser intensity across the density downramp and accordingly the wakefield strength play decisive roles in shaping $I(\xi)$.

For a clearer explanation, we first describe the simulation results presented in Fig. 2, where the notions of nonsaturated injection and saturated injection are introduced to facilitate further analysis of different injection processes and injected current distributions. We then explain in detail how the wakefield intensity influences the injection by tracking the injected particles to their initial positions in the plasma before they are influenced by the laser, similar to the discussion in Ref. 18. Finally, we investigate the relationship between the downramp parameters and the injected beam current and total charge.

A. Saturated and nonsaturated injection

The results of four simulations with different downramp positions Pos_d are reported in Fig. 2, where the plasma density before the downramp was fixed as $n_{\mathrm{high}} = 5 \times 10^{18}$ cm^{-3}, and the downramp length for all cases was $L = 40$ μm. The plot on the left of Fig. 2 shows the injected electron beam current distributions at the exit of the plasma and (as dashed lines in the inset) the normalized laser vector potential a_0 in the plasma density region of interest.

For larger values of Pos_d, the laser intensity across the downramp region increases, and the shape of the injected electron beam current $I(\xi)$ changes from triangle-like (the blue and orange lines in the left-hand plot in Fig. 2) to rectangle-like (the green line), and then to a piecewise function of two segments consisting of a peak and a constant segment (the red line).

As mentioned at the beginning of this section, the behavior of the beam current distribution depends mainly on the wakefield strength in the plasma density downramp. The higher the laser intensity, the stronger is the wakefield and the easier is the injection [a higher beam current $I(\xi)$]. Figures 2(a)–2(d) show the simulated plasma charge densities of the wakefields at positions in the middle of the corresponding density downramp. It can be seen that the bubble structure becomes clearer as Pos_d increases, which signifies a higher wakefield strength as well as system nonlinearity.

Here, for simplicity, we term the injection process where the wakefield reaches full blowout *saturated injection*, which results in the piecewise current shape (the red line in the left-hand plot in Fig. 2). The injection process without a full blowout wakefield is termed *nonsaturated injection*, which results in the triangle-like current shape (the blue and orange lines in Fig. 2). It should be noted that with the laser evolution and the change in plasma density across the downramp, the injection evolves from a nonsaturated process to a saturated one, corresponding to a rectangle-like current shape (the green line in Fig. 2). The underlying mechanisms are explained in detail in Sec. II B.

B. Distribution of initial positions of injected electrons

For a better understanding of how the laser and wakefield intensity influence the injection, we apply a similar approach to that adopted in Ref. 18 to investigate the initial positions (z_i, r_i) of the injected electrons before they are affected by the laser, using three different simulations corresponding to the orange, green, and red lines in the left-hand plot in Fig. 2. The case corresponding to the blue line in this plot is not shown here, since it shares the same physics as the case corresponding to the orange line. Electrons from the injected beam are traced back to their original positions in the plasma, and their distributions in the z_i–r_i plane are shown in Figs. 3(a)–3(c), where the downramp starts from 200, 300, and 400 μm, and ends at 240, 340, and 440 μm, respectively. The evolutions of a_0 in these regions are plotted as dashed black lines, from which it can be seen that a_0 increases for higher Pos_d. The distributions of linear charge density (the charge per unit length across z_i) over the longitudinal coordinate z, which we denote here by $\lambda_i(z_i)$, are plotted as red solid lines.

For complete *saturated injection*, as shown in Fig. 3(c) with a larger value of Pos_d, owing to nonlinear processes (such as relativistic self-focusing[20] or self-steepening effects[21] that increase with propagation distance), the blowout/bubble regime is valid throughout the downramp region, and the injected particles cover the whole downramp region (from 400 to 440 μm for the case considered here). A small proportion of the particles before the downramp region ($z_i < 400$ μm) are also involved in the injection process. An accumulation of charge is observed at the beginning of the downramp, and this results in a charge density peak, probably due to the rapid changes in wakefield structure, which causes extra particles to be injected, smoothing the peak to a lower value with a slightly rounded beginning of the density downramp. A constant $\lambda_i(z_i)$ is found just after the peak, which can be explained by the negligible evolution of a_0, and accordingly the wakefield strength, across the plasma downramp. Actually, the supposition that a fixed driver intensity results in a relatively constant $\lambda_i(z_i)$ is also supported by a study of the downramp injection in PWFA,[18] which indicates that only particles initially situated around a thin sheet near a fixed transverse position $r_i \simeq \kappa r_m$ are able to be injected, where r_m is the maximum transverse radius of the bubble and $\kappa \simeq 1$ is a nondimensional value.

For $\mathrm{Pos}_d = 200$ μm, as shown in Fig. 3(a), where the wakefield is still weak, only *nonsaturated injection* occurs, and it does so at a position closer to the rear of the downramp where a_0 is strong enough to trigger injection, corresponding to a triangle-like shape of $\lambda_i(z_i)$. For $\mathrm{Pos}_d = 300$ μm, the wakefield strength is slightly below the blowout regime, and nearly saturated injection occurs approaching the end of the downramp, with $\lambda_i(z_i)$ exhibiting a trapezoidal shape. In these two cases, particles with smaller initial transverse positions (nearer to the axis) are also involved in the injection process. These particles are accelerated and injected inside the wakefield without going along the sheath of bubbles in the plasma wake.

The beam charge density distributions in the ξ–z_i plane, together with the beam current shapes, are shown in Figs. 3(d)–3(f), corresponding to $\mathrm{Pos}_d = 200$, 300, and 400 μm, respectively. Along almost the whole bunch duration, a nearly linear correlation is observed between the initial longitudinal position z_i and the injected phase position ξ. This near-linearity indicates that the dependence of $\lambda_i(z_i)$ on z_i has a similar shape to the dependence of the final beam current $I(\xi)$ on ξ, as can be seen by comparing Figs. 3(a)–3(c) with Figs. 3(d)–3(f), respectively. This correspondence in the case of PWFA is explained in Ref. 18. It should be mentioned that the nearly one-to-one mapping is also valid for LWFA under the condition that there is little evolution of a_0 across the density downramp, which holds for the cases reported here.

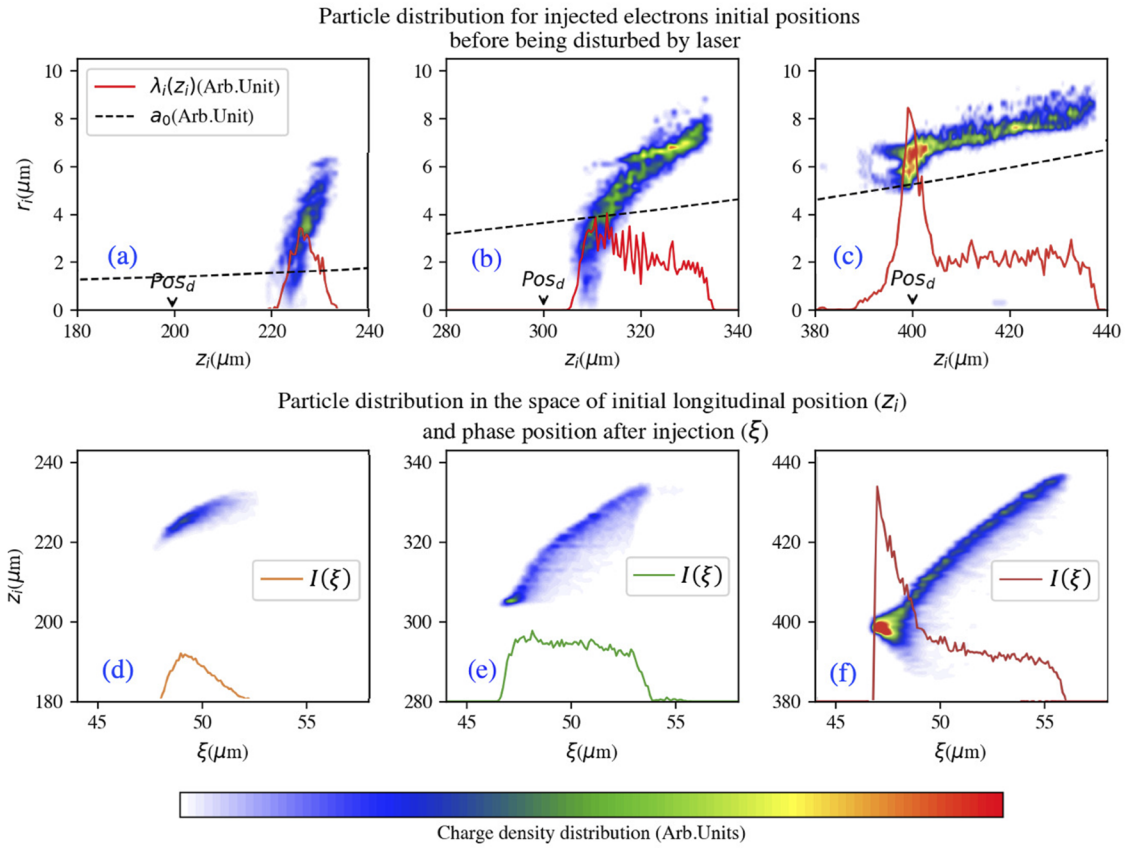

FIG. 3. (a)–(c) Particle distributions of injected particles in the z_i–r_i plane at their initial positions before being disturbed by the laser for each simulation. (d)–(f) Particle distributions in the space constructed from their initial longitudinal position z_i and the phase position in the wakefield after the injection ξ.

C. Relationship between plasma density parameters and injected beam current

To investigate the effect of the density gradient on the beam parameters, we performed another series of simulations for different downramp lengths L. Figure 4 shows the beam current distributions for four different values of the density gradient and four different downramp positions Pos_d. For cases with *nonsaturated injection*, the steeper the downramp (i.e., the smaller the value of L), the easier the injection becomes. When the wakefield across the plasma density downramp is relatively weak (corresponding to small Pos_d), no injection at all occurs for large L. From the results shown here, no injection is observed for L = 60 and 75 μm when Pos_d is set as 100 μm.

For cases with *saturated injection*, the value of the constant part of the current profile is barely influenced by the downramp length L, as can be seen by comparing the red lines in Fig. 4 near the tail of the injected beam. Further evidence for this is provided by the simulation results shown in Fig. 4(b), where similar beam currents near the tail of the bunch are observed for different values of the downramp steepness.

Simulations (not reported here) were also performed with different values of n_{high} but the same n_{low}. For the full blowout situations across the downramp region, the injected beam is observed to have a longer duration with higher plasma density before the downramp, which potentially increases the beam charge Q. This has also been observed in Ref. 24, and the reason is that the bubble size in the high-density region is smaller for higher n_{high}, as a consequence of which the head of the injected electron bunch moves closer to the laser driver, while its tail stays at the rear of the bubble. However, Q is also limited by the acceleration capacity of the structure after the downramp, as discussed in Sec. IV.

It is interesting to calculate the total injected charge $Q = (1/c)\int_{\mathrm{beam}} I(\xi)\,\mathrm{d}\xi$ produced by each set of plasma parameters. Figure 5 shows the variation of the beam charge Q with the downramp length L for four downramp positions Pos_d, similar to Fig. 2. The majority of the bunches are injected without reaching saturation for smaller Pos_d, corresponding to the blue, orange, and green lines here. A decrease in Q is observed with decreasing downramp steepness when the value of L is relatively small. The charge Q increases after a certain value of L, because the end of the downramp

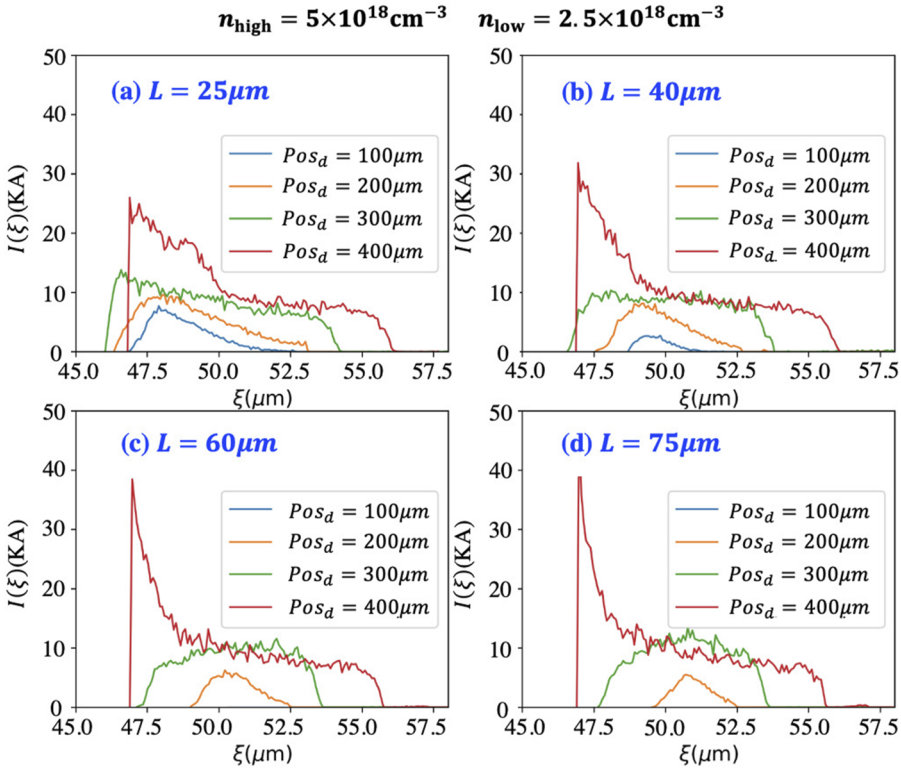

FIG. 4. Beam sliced currents for fixed $n_{high} = 5 \times 10^{18}$ cm^{-3} and different downramp lengths L and downramp positions Pos$_d$.

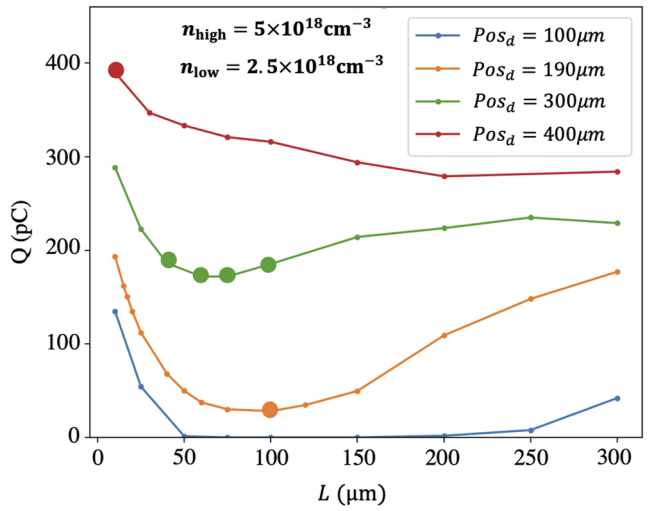

FIG. 5. Beam charge Q for fixed $n_{high} = 5 \times 10^{18}$ cm^{-3} with different downramp lengths L and downramp positions Pos$_d$.

sees an increase in laser intensity a_0, which results in more injected particles. For cases with saturated injection, corresponding to the red line here, Q decreases at larger L. The data represented by the large dots correspond to the cases with optimal energy performance, which will be discussed in Sec. III.

III. CONTROL OF BEAM ENERGY EVOLUTION AND OPTIMIZATION OF BEAM PARAMETERS

The results of a typical simulation of the production of monoenergetic beams with energies of hundreds of MeV for initial plasma density parameters $n_{high} = 5 \times 10^{18}$ cm^{-3}, Pos$_d$ = 300 μm, and $L = 40$ μm are presented here. The evolution of the electron beam energy is shown in Fig. 6(a), where the energy spectrum for the injected bunch with respect to the propagation distance is presented as a color map. The mean energy of the beam is plotted as a red solid line (with values given on the left vertical axis) and the absolute energy spread of the beam δE is plotted as a green dashed line (with values given on the right vertical axis). The current $I(\xi)$ of the injected beam in this simulation corresponds to the green line in the left-hand plot in Fig. 2.

As the beam propagates, its energy spread reaches a minimum value before increasing again. To understand the reason for this energy evolution, the electron beam density distributions in longitudinal phase space (the z–E plane) at different propagation distances, as well as the acceleration force, are plotted in Figs. 6(b)–6(d). It can be seen from the very thin beam profiles in longitudinal phase space that the large energy spreads are due to energy chirping, whereas the sliced energy spreads remain low throughout the propagation. The beam chirps negatively (the tail has a higher energy than the head of the bunch) at the beginning of the simulation and then flattens during its propagation before taking a nearly horizontal shape (with the head and tail of the beam holding nearly the same energy). The nearly horizontal shape is where the minimum energy spread is found. The chirp then turns positive and increases continuously

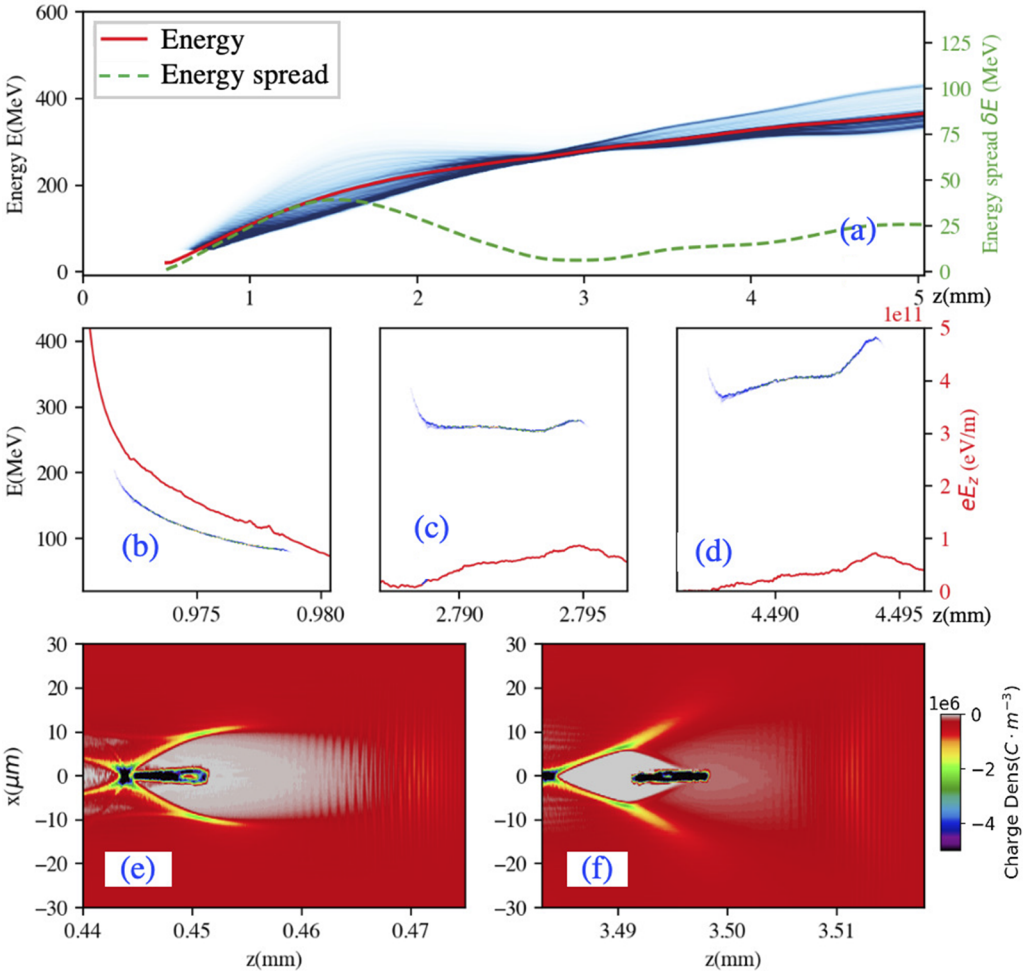

FIG. 6. (a) Evolution of beam energy with propagation distance for a simulation with $n_{high} = 5 \times 10^{18}$ cm^{-3}, Pos$_d$ = 300 μm, and L = 40 μm. (b)–(d) Beam profiles in longitudinal phase space for different propagation distances, where the red lines show the on-axis acceleration forces. (e) and (f) Wakefields for two different propagation distances.

until the end of the simulation, and the energy spread increases correspondingly. Here, we define the optimized propagation distance to be the zone where the minimum energy spread (also the minimum relative energy spread, because for longer propagation distance the beam energy does not increase significantly in this group of simulations) is obtained. Here, we focus on three elements that characterize the evolution of the beam energy: (i) the minimum energy spread $\min(\delta E)$; (ii) the beam mean energy, at which the minimum energy spread reaches $E(\min(\delta E))$; (iii) the rate $\mathrm{d}(\delta E)/\mathrm{d}z$ at which δE increases after its minimum.

The evolution of the beam profile in longitudinal phase space is a result of the evolution of the acceleration force $F_{acc}(z)$ to which the beam is subjected at different longitudinal positions. This is a combined effect of the laser wakefield and the beam's self-loaded wakefield. Shortly after the bunch has been injected, the acceleration force to which the tail of the beam is subjected is stronger than that at its front, which results in the negative chirp. As the wakefield structure propagates in the plasma, the acceleration force weakens owing to laser depletion. Accordingly, the beam's self-loaded wakefield, which exerts a decelerating effect, becomes more pronounced at the rear of the beam. As a result, the head of the bunch is subjected to a stronger acceleration field than the tail. The wakefield structures shortly after the downramp and near a propagation distance of 3.5 mm are illustrated in Figs. 6(e) and 6(f), respectively. It can be seen that the wakefield contributed by the laser (the fine periodic structure before the beam head in the figure) becomes much weaker after a few millimeters of propagation, and thus the beam's self-loaded wakefield starts to have a stronger effect.

As explained in Ref. 30, one can shape the acceleration force by modifying the beam current $I(\xi)$. Since the beam current profile $I(\xi)$ can be tailored by tuning the plasma density parameters as mentioned in Sec. II, the beam energy performance can be optimized

by tuning the four main parameters of the plasma profile: n_{high}, n_{low}, L, and Pos_d.

We performed a series of simulations to map the relationship between the plasma parameters and the evolution of the beam energy. The first group of simulations corresponds to the green line in Fig. 5, for which $n_{high} = 5 \times 10^{18}$ cm^{-3} and the downramp position is $Pos_d = 300$ μm. Only the downramp length L varies. The evolution of the energy spread δE with propagation is plotted for several cases in this group in Fig. 7(a). The profiles of the energy evolution for the whole beam are plotted in Fig. 7(b). The black dots outline the zones of interest where the minimum energy spreads $\min(\delta E)$ are reached. The plasma density profiles and the evolution of a_0 are illustrated in Fig. 7(c).

The beam currents $I(\xi)$ for three cases in this group are plotted in Fig. 7(d). Note that according to the analysis in Sec. II, there is a transition of the injection process from nonsaturated to saturated. With a steeper downramp (smaller L), the current behavior changes from a decreasing trend to a slightly increasing trend. As L continues to increase, an accumulation of particles is again found at the head of the bunch.

The minimum energy spread is very sensitive to the beam current, which takes different forms for different downramp gradients (different values of L). The value of $\min(\delta E)$ decreases at larger L and reaches its lowest value for the simulations in this group when $L = 60$ μm, as shown in Fig. 7(a). As L continues to increase, the beam energy obtained in the optimized zone for beam delivery, $E(\min(\delta E))$, decreases [Fig. 7(b)]. Meanwhile, the speed at which δE evolves after the zone of delivery, $\mathrm{d}(\delta E)/(d)z$, is higher, which makes the system more sensitive to experimental control.

We are also interested in the relationships between the achievable δE, E, and Q, which we consider to be the three main parameters characterizing the injected beam, and these are presented in Fig. 7(e), where the downramp length L increases in the direction of the arrow. For given values of $E(\min(\delta E))$ on the horizontal axis and $\min(\delta E)$ on the vertical axis, the corresponding beam charges Q in picocoulombs are shown in the circles. It can be seen that the achievable minimum energy spread coincides with the attainable maximum energies [the right-most charges in Fig. 7(e) are also the lowest], which is favorable for the production of high-energy monoenergetic beams. Table I presents the final beam parameters of four cases in

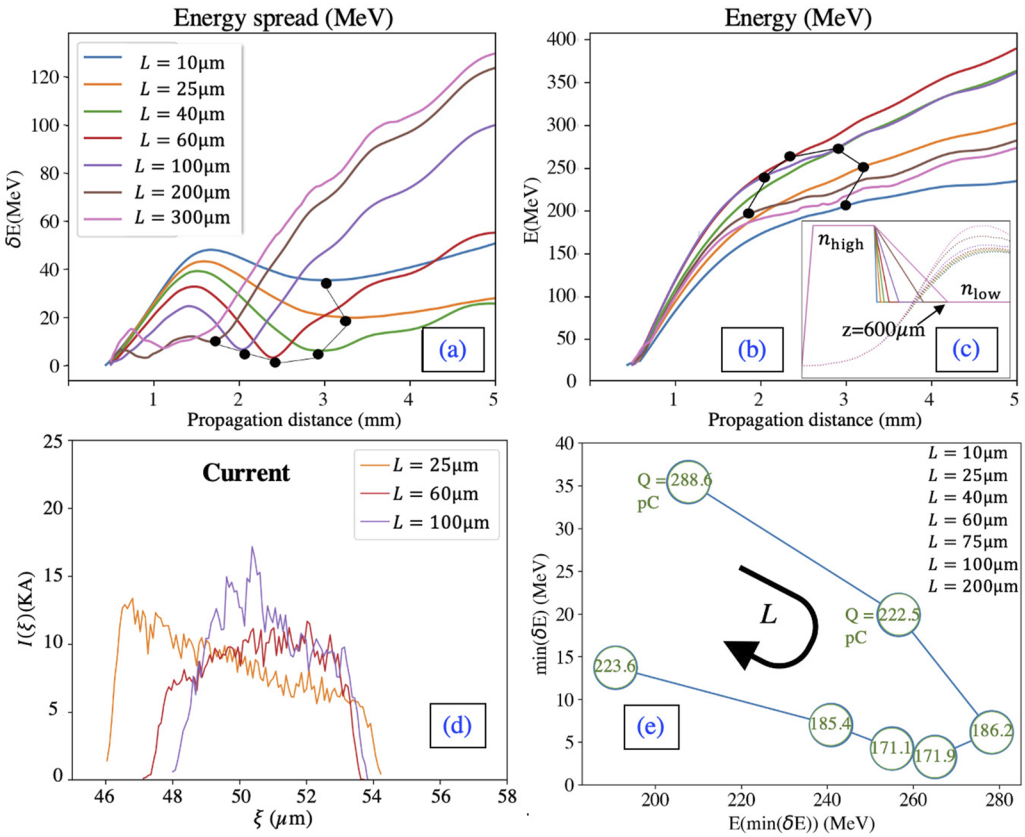

FIG. 7. (a) and (b) Evolution of δE and E, respectively, for fixed $Pos_d = 300$ μm and $n_{high} = 5 \times 10^{18}$ cm^{-3} and different values of L. The black dots outline the optimized zones. (c) Plasma density and evolution of the laser a_0. (d) Beam currents for three of the values of L. (e) Relationships between minimum energy spread, energy, and injected beam charge for different values of L (increasing in the direction of the arrow), with the charge values encircled for each point.

TABLE I. Plasma parameters and final beam parameters for the optimum cases that give the smallest $\delta E/E$ for each group of simulations.

	Plasma parameters				Final beam parameters			
Simulation group	n_{high} (cm^{-3})	n_{low} (cm^{-3})	L (μm)	Pos_d (μm)	Q (pC)	δE (MeV)	E (MeV)	$\delta E/E$ (%)
1	5×10^{18}	2.5×10^{18}	40	300	186.2	6.20	278.14	2.2
	5×10^{18}	2.5×10^{18}	60	300	171.5	3.31	265.02	1.2
	5×10^{18}	2.5×10^{18}	75	300	171.1	4.32	255.03	1.7
	5×10^{18}	2.5×10^{18}	100	300	185.4	7.05	240.82	2.9
2	5×10^{18}	2.5×10^{18}	100	190	28.0	10.22	993.2	1.03
3	5×10^{18}	2.5×10^{18}	10	400	390.1	7.70	144.5	5.3

this group that are considered to be optimal in the context of obtaining high-energy monoenergetic beams, i.e., those with the smallest $\delta E/E$ values.

The second group of simulations corresponds to the orange line in Fig. 5, for which $n_{high} = 5\times10^{18}$ cm^{-3}, and $Pos_d = 190$ μm. The evolution of the beam parameters is plotted for some cases in this group in Fig. 8. Further investigations with longer propagation distances are performed for those simulations of interest in which δE is conserved or increases only slowly when 5 mm propagation is reached, corresponding to the cases with $L = 75$, 100, and 120 μm. As shown in Fig. 8(c), the relative energy spreads are only a few percent where the beam peak energies reach approximately their maximum, ~1 GeV. Beam currents for five of these cases are plotted in Fig. 8(b). For this simulation group, the current shape is pulse-like. Similar to the first simulation group, the current moves further to the rear of the bubble with larger downramp length L, and the beam length decreases significantly. The energy spread is roughly conserved only for weak beam current and thus low charge Q. This conservation of energy spread is possible because of the short beam lengths and weak current strength, as a consequence of which the beam loading is not significant and the wakefield driven by the laser is dominant throughout the propagation. The high energy gain, on the other hand, is due to the fact that the drive laser reaches a self-guided condition and provides a stable wakefield for a long propagation distance.[28] The beam charges Q for the cases of interest are around 30 pC. The parameters of the best case of this group are presented in Table I.

We now focus on the third group of simulations, which corresponds to the red line in Fig. 5. The energy evolution is presented for several cases in this group in Fig. 9. Only saturated

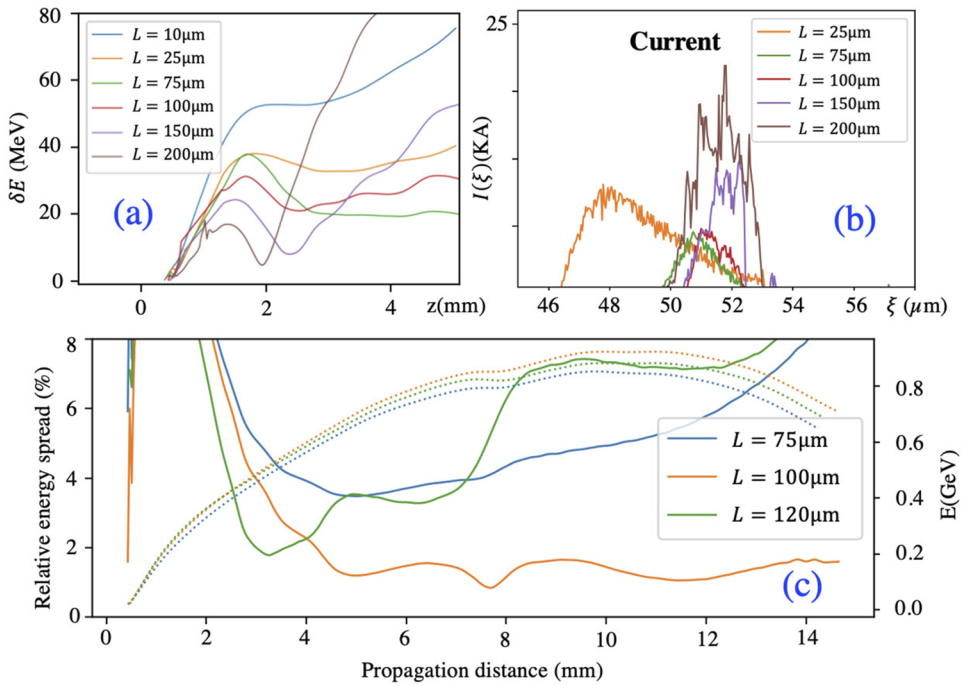

FIG. 8. (a) Energy spread as a function of the propagation distance for six values of the downramp gradient. (b) Corresponding beam currents. (c) Relative energy spread and energy as functions of the propagation distance for a set of four values of the downramp gradient.

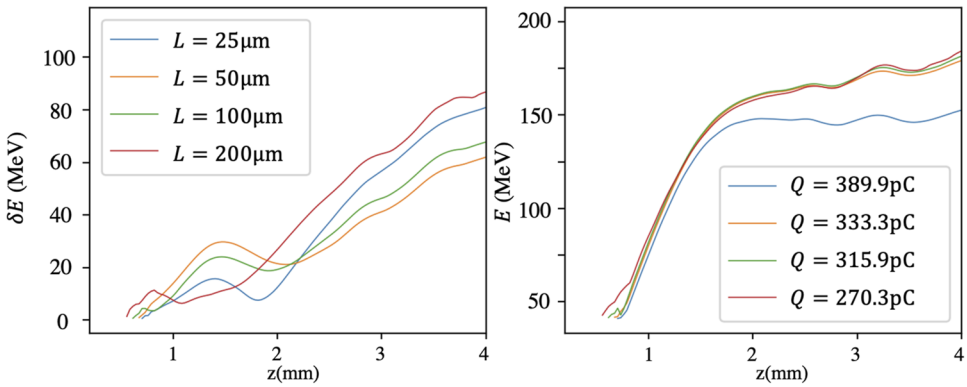

FIG. 9. Energy spread and energy evolution for $Pos_d = 400\ \mu m$ and four values of the downramp density gradient.

injection occurs for this simulation group. The beams are barely accelerated after reaching 150 MeV. Similar to the other simulation groups, the optimized beam delivery zone is where the minimum energy spread is reached. Among all the simulations in this group, the most monoenergetic case is found to be that with the smallest L, for which the injected beam charge approaches 390 pC.

The simulations presented in this section have mostly used the same plasma densities n_{high} and n_{low}. With different n_{high}, as discussed in Sec. II, nearly identical beam currents can be obtained, which means similar beam energy evolutions.

IV. LIMITS ON ACCELERATION CAPACITY

The beam charge that can be accelerated is limited by the wakefield amplitude and depends on the laser evolution after the downramp and the plasma density n_{low}. We call this limit the *deceleration* limit.

When the beam current and accordingly the total beam charge are sufficiently high, the decelerating wakefield caused by the beam itself becomes so strong that the majority of particles in the beam are decelerated. The energy spectrum for a simulation that exceeds this deceleration limit is shown in Fig. 10(a), and the corresponding beam profiles in longitudinal phase space at two different propagation distances are illustrated in Figs. 10(b) and 10(c). The initial plasma parameters of this simulation are $n_{high} = 5 \times 10^{18}\ cm^{-3}$, $Pos_d = 435\ \mu m$, and $L = 25\ \mu m$. The injected charge is 394.4 pC.

Among all the performed simulations, the maximum injected charge obtained is 454.2 pC, for $n_{high} = 1 \times 10^{19}\ cm^{-3}$, $Pos_d = 225\ \mu m$, and $L = 25\ \mu m$. The beam current is nearly flat, which makes the energy spread relatively stable during propagation, as shown in Fig. 11.

Increasing n_{high} is not helpful in reaching a higher beam charge, because the bunch length cannot exceed the acceleration and focusing part of the bubble structure. One can expect that lowering n_{low} for a larger bubble structure should enable longer bunches to be accelerated. Further mappings of the achievable beam charge Q and plasma parameters are not presented here, because the beam energy performance for saturated injected beams is not optimal in the context of obtaining a monoenergetic and highly charged beam.

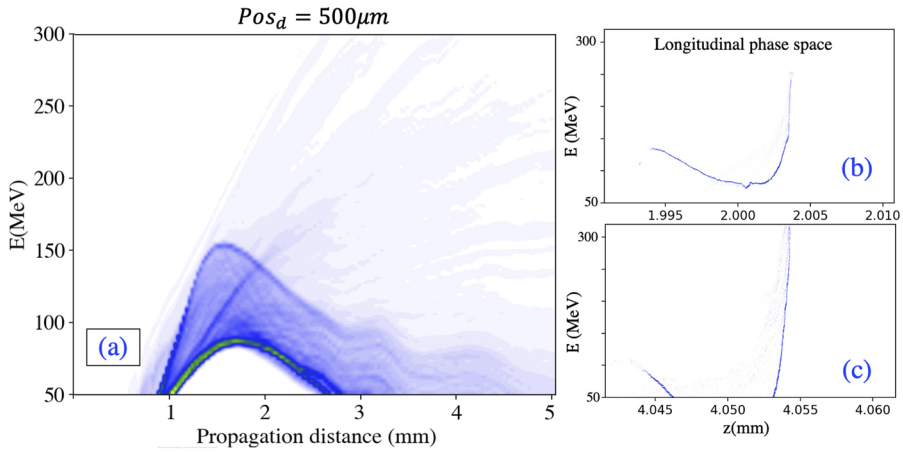

FIG. 10. (a) Energy spectrum. (b) and (c) Longitudinal phase space at two different propagation distances. The initial plasma parameters are $n_{high} = 5 \times 10^{18}\ cm^{-3}$, $L = 25\ \mu m$, and $Pos_d = 500\ \mu m$. Significant particle loss is observed after 3 mm of propagation.

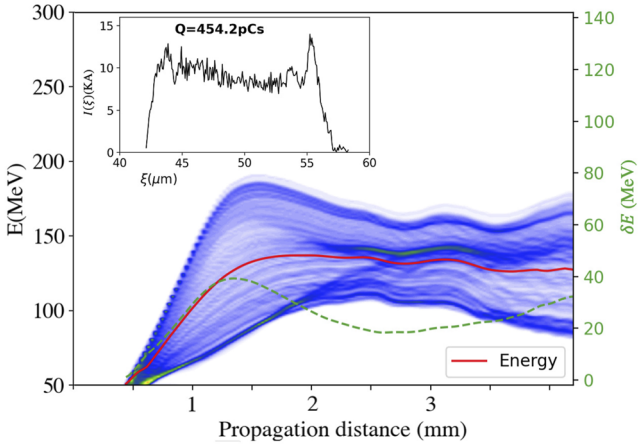

FIG. 11. Energy spectrum for the simulation with initial plasma parameters $n_{high} = 1 \times 10^{19}$ cm^{-3}, $L = 25$ μm, and Pos$_d$ = 225 μm. The inset shows the beam current for this simulation.

V. CONCLUSIONS

A systematic and comprehensive study on obtaining high-quality electron beams using the density downramp injection technique in a one-stage laser wakefield accelerator has been presented, and it has been shown how the plasma target parameters affect the beam performances.

It is understood that the beam current $I(\xi)$ is of decisive importance not only for obtaining a desirable beam charge but also for the beam energy evolution. The current profile can be tailored by adjusting the position of the plasma downramp region, taking account of the local laser intensity. Different current profiles $I(\xi)$ give rise to different energy evolution patterns. The achievable beam charge for a fixed $n_{low} = 2.5 \times 10^{18}$ cm^{-3} varies from 0 to 450 pC. The beams with the highest charge and variable current shapes can potentially be tuned and adapted to provide suitable driver beams for high-transformer-ratio PWFA.[15,25]

For injected charges on the scale of hundreds of picocoulombs, a minimum energy spread min(δE) is found as a result of the competition between the self-loaded decelerating field and the evolution of the accelerating wakefield driven by the laser during propagation. The optimum zones for beam delivery are those where min(δE) is reached. Beams with charges over 170 pC, energies in the 200 MeV range, and less than 2% relative energy spread are obtained, and these suit nicely the requirements for radiotherapy applications with very high-energy electrons (VHEE).[31–33]

For cases where relatively low charge is injected, conservation of the energy spread over long propagation distances is observed, which permits very high beam energies (~1 GeV) to be reached with less than 2% energy spread. Such cases can be further tuned and adapted to free-electron laser applications that have recently been demonstrated.[16]

In the context of downramp injection, we have presented qualitative relationships between output beam parameters and input laser–plasma parameters that can provide guidance for future experiments conducted with the laser systems of a few tens of terawatts that are available in many laboratories. These are general relationships, and the determination of precise parameter values will require further studies to answer the varying requirements of different applications and available experimental conditions.

ACKNOWLEDGMENTS

This work was supported by the Fondation Jacques Toledano and the Schwartz-Reisman Center for Intense Laser Physics, and by ERC PoC Vherapy and EIC ebeam4therapy grants.

AUTHOR DECLARATIONS

Conflict of Interest

The authors have no conflicts to disclose.

Author Contributions

Céline S. Hue: Conceptualization (equal); Data curation (equal); Investigation (equal); Methodology (equal); Visualization (equal); Writing – original draft (equal). **Yang Wan**: Conceptualization (equal); Investigation (equal); Methodology (equal); Supervision (equal); Validation (equal); Writing – review & editing (equal). **Eitan Y. Levine**: Investigation (equal). **Victor Malka**: Conceptualization (supporting); Funding acquisition (lead); Methodology (supporting); Project administration (lead); Supervision (lead); Validation (supporting); Writing – review & editing (lead).

DATA AVAILABILITY

In this article, all numerical simulations are performed with the quasi-3D particle-in-cell (PIC) code FBPIC,[26] where the algorithm is based on Fourier–Bessel decomposition of fields on a set of 2D radial grids. Here an example input file for launching the simulation is attached. The concerned parameters for each simulation are indicated percisely in the article.

REFERENCES

[1]T. Tajima and J. M. Dawson, "Laser electron accelerator," Phys. Rev. Lett. **43**, 267–270 (1979).
[2]E. Esarey, C. B. Schroeder, and W. P. Leemans, "Physics of laser-driven plasma-based electron accelerators," Rev. Mod. Phys. **81**, 1229 (2009).
[3]V. Malka, "Laser plasma accelerators," Phys. Plasmas **19**, 055501 (2012).
[4]S. Kalmykov, S. A. Yi, V. Khudik, and G. Shvets, "Electron self-injection and trapping into an evolving plasma bubble," Phys. Rev. Lett. **103**, 135004 (2009).
[5]I. Kostyukov, E. Nerush, A. Pukhov, and V. Seredov, "Electron self-injection in multidimensional relativistic-plasma wake fields," Phys. Rev. Lett. **103**, 175003 (2009).
[6]D. H. Froula, C. E. Clayton, T. Döppner, K. A. Marsh, C. P. J. Barty, L. Divol, R. A. Fonseca, S. H. Glenzer, C. Joshi, W. Lu *et al.*, "Measurements of the critical power for self-injection of electrons in a laser wakefield accelerator," Phys. Rev. Lett. **103**, 215006 (2009).
[7]S. P. Mangles, G. Genoud, M. S. Bloom, M. Burza, Z. Najmudin, A. Persson, K. Svensson, A. G. R. Thomas, and C.-G. Wahlström, "Self-injection threshold in self-guided laser wakefield accelerators," Phys. Rev. Spec. Top.–Accel. Beams **15**, 011302 (2012).
[8]Y. Wan, O. Seemann, S. Tata, I. A. Andriyash, S. Smartsev, E. Kroupp, and V. Malka, "Direct observation of relativistic broken plasma waves," Nat. Phys. **18**, 1186–1190 (2022).

[9]C. McGuffey, A. G. Thomas, W. Schumaker, T. Matsuoka, V. Chvykov, F. J. Dollar, G. Kalintchenko, V. Yanovsky, A. Maksimchuk, K. Krushelnick *et al.*, "Ionization induced trapping in a laser wakefield accelerator," Phys. Rev. Lett. **104**, 025004 (2010).
[10]A. Pak, K. A. Marsh, S. F. Martins, W. Lu, W. B. Mori, and C. Joshi, "Injection and trapping of tunnel-ionized electrons into laser-produced wakes," Phys. Rev. Lett. **104**, 025003 (2010).
[11]B. B. Pollock, C. E. Clayton, J. E. Ralph, F. Albert, A. Davidson, L. Divol, C. Filip, S. H. Glenzer, K. Herpoldt, W. Lu *et al.*, "Demonstration of a narrow energy spread, ~0.5 GeV electron beam from a two-stage laser wakefield accelerator," Phys. Rev. Lett. **107**, 045001 (2011).
[12]S. Bulanov, N. Naumova, F. Pegoraro, and J. Sakai, "Particle injection into the wave acceleration phase due to nonlinear wake wave breaking," Phys. Rev. E **58**, R5257–R5260 (1998).
[13]K. Schmid, A. Buck, C. M. S. Sears, J. M. Mikhailova, R. Tautz, D. Herrmann, M. Geissler, F. Krausz, and L. Veisz, "Density-transition based electron injector for laser driven wakefield accelerators," Phys. Rev. Spec. Top.–Accel. Beams **13**, 091301 (2010).
[14]A. Buck, J. Wenz, J. Xu, K. Khrennikov, K. Schmid, M. Heigoldt, J. M. Mikhailova, M. Geissler, B. Shen, F. Krausz, S. Karsch, and L. Veisz, "Shock-front injector for high-quality laser-plasma acceleration," Phys. Rev. Lett. **110**, 185006 (2013).
[15]F. M. Foerster, A. Döpp, F. Haberstroh, K. v. Grafenstein, D. Campbell, Y.-Y. Chang, S. Corde, J. P. Couperus Cabadağ, A. Debus, M. F. Gilljohann, A. F. Habib, T. Heinemann, B. Hidding, A. Irman, F. Irshad, A. Knetsch, O. Kononenko, A. Martinez de la Ossa, A. Nutter, R. Pausch, G. Schilling, A. Schletter, S. Schöbel, U. Schramm, E. Travac, P. Ufer, and S. Karsch, "Stable and high-quality electron beams from staged laser and plasma wakefield accelerators," Phys. Rev. X **12**, 041016 (2022).
[16]W. Wang, K. Feng, L. Ke, C. Yu, Y. Xu, R. Qi, Y. Chen, Z. Qin, Z. Zhang, M. Fang, J. Liu, K. Jiang, H. Wang, C. Wang, X. Yang, F. Wu, Y. Leng, J. Liu, R. Li, and Z. Xu, "Free-electron lasing at 27 nanometres based on a laser wakefield accelerator," Nature **595**, 516–520 (2021).
[17]H. Suk, N. Barov, J. B. Rosenzweig, and E. Esarey, "Plasma electron trapping and acceleration in a plasma wake field using a density transition," Phys. Rev. Lett. **86**, 1011 (2001).
[18]X. L. Xu, F. Li, W. An, T. N. Dalichaouch, P. Yu, W. Lu, C. Joshi, and W. B. Mori, "High quality electron bunch generation using a longitudinal density-tailored plasma-based accelerator in the three-dimensional blowout regime," Phys. Rev. Accel. Beams **20**, 111303 (2017).
[19]A. M. de la Ossa, Z. Hu, M. Streeter, T. Mehrling, O. Kononenko, B. Sheeran, and J. Osterhoff, "Optimizing density down-ramp injection for beam-driven plasma wakefield accelerators," Phys. Rev. Accel. Beams **20**, 091301 (2017).
[20]G.-Z. Sun, E. Ott, Y. C. Lee, and P. Guzdar, "Self-focusing of short intense pulses in plasmas," Phys. Fluids **30**, 526–532 (1987).
[21]J. Vieira, F. Fiúza, L. O. Silva, M. Tzoufras, and W. B. Mori, "Onset of self-steepening of intense laser pulses in plasmas," New J. Phys. **12**, 045025 (2010).
[22]S. A. Samant, A. K. Upadhyay, and S. Krishnagopal, "High brightness electron beams from density transition laser wakefield acceleration for short-wavelength free-electron lasers," Plasma Phys. Controlled Fusion **56**, 095003 (2014).
[23]F. Massimo, A. F. Lifschitz, C. Thaury, and V. Malka, "Numerical studies of density transition injection in laser wakefield acceleration," Plasma Phys. Controlled Fusion **59**, 085004 (2017).
[24]H. Ekerfelt, M. Hansson, I. Gallardo González, X. Davoine, and O. Lundh, "A tunable electron beam source using trapping of electrons in a density down-ramp in laser wakefield acceleration," Sci. Rep. **7**, 12229 (2017).
[25]T. Kurz, T. Heinemann, M. F. Gilljohann, Y. Y. Chang, J. P. Couperus Cabadağ, A. Debus, O. Kononenko, R. Pausch, S. Schöbel, R. W. Assmann *et al.*, "Demonstration of a compact plasma accelerator powered by laser-accelerated electron beams," Nat. Commun. **12**, 2895 (2021).
[26]R. Lehe, M. Kirchen, I. A. Andriyash, B. B. Godfrey, and J.-L. Vay, "A spectral, quasi-cylindrical and dispersion-free particle-in-cell algorithm," Comput. Phys. Commun. **203**, 66–82 (2016).
[27]E. Kroupp, S. Tata, Y. Wan, D. Levy, S. Smartsev, E. Y. Levine, O. Seemann, M. Adelberg, R. Piliposian, T. Queller, E. Segre, K. Ta Phuoc, M. Kozlova, and V. Malka, "Commissioning and first results from the new 2 × 100 TW laser at the WIS," Matter Radiat. Extremes **7**, 044401 (2022).
[28]W. Lu, M. Tzoufras, C. Joshi, F. S. Tsung, W. B. Mori, J. Vieira, R. A. Fonseca, and L. O. Silva, "Generating multi-GeV electron bunches using single stage laser wakefield acceleration in a 3D nonlinear regime," Phys. Rev. Spec. Top.–Accel. Beams **10**, 061301 (2007).
[29]C. Thaury, E. Guillaume, A. Lifschitz, K. Ta Phuoc, M. Hansson, G. Grittani, J. Gautier, J.-P. Goddet, A. Tafzi, O. Lundh, and V. Malka, "Shock assisted ionization injection in laser-plasma accelerators," Sci. Rep. **5**, 16310 (2015).
[30]M. Tzoufras, W. Lu, F. S. Tsung, C. Huang, W. B. Mori, T. Katsouleas, J. Vieira, R. A. Fonseca, and L. O. Silva, "Beam loading in the nonlinear regime of plasma-based acceleration," Phys. Rev. Lett. **101**, 145002 (2008).
[31]Y. Glinec, J. Faure, V. Malka, T. Fuchs, H. Szymanowski, and U. Oelfke, "Radiotherapy with laser-plasma accelerators: Monte Carlo simulation of dose deposited by an experimental quasimonoenergetic electron beam," Med. Phys. **33**, 155–162 (2006).
[32]T. Fuchs, H. Szymanowski, U. Oelfke, Y. Glinec, C. Rechatin, J. Faure, and V. Malka, "Treatment planning for laser-accelerated very-high energy electrons," Phys. Med. Biol. **54**, 3315–3328 (2009).
[33]V. Malka, J. Faure, Y. A. Gauduel, E. Lefebvre, A. Rousse, and K. T. Phuoc, "Principles and applications of compact laser–plasma accelerators," Nat. Phys. **4**, 447–453 (2008).